JOURNAL OF THERMOPHYSICS AND HEAT TRANSFER
Vol. 25, No. 3, July–September 2011

Mixed Electroosmotically and Pressure-Driven Flow with Temperature-Dependent Properties

Arman Sadeghi,* Hadi Yavari,† and Mohammad Hassan Saidi‡
Sharif University of Technology, 11365-11555 Tehran, Iran
and
Suman Chakraborty§
Indian Institute of Technology, Kharagpur 721302, India

DOI: 10.2514/1.T3638

The present work reports the outcome of a comprehensive parametric study on mixed electroosmotically and pressure-driven flow in slit microchannels with constant wall heat fluxes. Special attention is given to disclose the applicability ranges of usual assumptions in simplified analyses. The governing equations for fully developed conditions are first made dimensionless and then solved by means of an implicit finite difference method. The results reveal that the assumption of constant thermophysical properties does not lead to significant errors in practical applications. Although the Debye–Huckel linearization may successfully be used to evaluate velocity profiles up to the zeta potentials of 50 mV, nevertheless, the calculated Poiseuille numbers may be quite different from the exact ones, even for lower zeta potentials. It is also found that this linearization may fail at predicting accurate velocity profiles when a considerable amount of opposed pressure exists, even at very low zeta potentials. Unless a sufficiently high value of the dimensionless Debye–Huckel parameter is considered, assuming a uniform distribution for the Joule heating leads to large errors in calculating the thermal aspects for the zeta potentials of more than 25 mV. Furthermore, increasing the zeta potential leads to decreasing the viscous heating effects at lower values of the dimensionless Debye–Huckel parameter, whereas the opposite is true for higher amounts of this parameter.

Nomenclature

A	=	viscosity variation parameter, $\gamma\lambda_D^2 E_x^2/k\sigma_{0,w}$
B	=	electrical resistivity variation parameter, $\beta\lambda_D^2 E_x^2/k\sigma_{0,w}$
Br	=	Brinkman number, $SS_v u_m^{*2}/K^2$
c_p	=	specific heat at constant pressure, kJ kg^{-1} K^{-1}
D_h	=	hydraulic diameter of channel, $4H$
E_J	=	total Joule heating per channel length, $HI_1 E_x^2/\sigma_{0,w}$
E_v	=	total viscous heating per channel length, $\mu_w I_2 u_{\mathrm{HS}}^2/H$
E_x	=	electric field in the axial direction Vm^{-1}
e	=	proton charge, C
$\mathbf{F}$	=	body force vector, Nm^{-3}
f	=	friction factor, $2\tau_{xy,w}/\rho u_m^2$
H	=	channel half-height, m
h	=	heat transfer coefficient Wm^{-2} K^{-1}
k	=	thermal conductivity, Wm^{-1} K^{-1}
k_B	=	Boltzmann constant, JK^{-1}
Nu	=	Nusselt number, hD_h/k
n	=	number of grid points
n_0	=	ion density, m^{-3}
p	=	pressure, Pa
q	=	wall heat flux, Wm^{-2}
Re	=	Reynolds number, $\rho u_m D_h/\mu_w$
S	=	dimensionless Joule heating parameter, $E_x^2 H/q\sigma_{0,w}$
S_v	=	dimensionless viscous heating parameter, $\mu_w\sigma_{0,w}u_{\mathrm{HS}}^2/E_x^2\lambda_D^2$
s	=	volumetric heat generation due to Joule heating, Wm^{-3}
T	=	temperature, K
t	=	time, s
u	=	axial velocity, ms^{-1}
$\mathbf{u}$	=	velocity vector, ms^{-1}
u_{HS}	=	Helmholtz–Smoluchowski velocity, $-\varepsilon\zeta E_x/\mu_w$
u_{PD}	=	pressure-driven velocity, $-H^2(\mathrm{d}p/\mathrm{d}x)/2\mu_w$
u^*	=	dimensionless axial velocity, u/u_{HS}
x	=	axial coordinate, m
y	=	transverse coordinate, m
y^*	=	dimensionless transverse coordinate, y/H
z	=	valence number of ions in solution
β	=	constant, Eq. (18)
Γ	=	velocity scale ratio, $u_{\mathrm{PD}}/u_{\mathrm{HS}}$
γ	=	constant, Eq. (17)
δ	=	length over which a velocity gradient exists, m
ε	=	fluid permittivity, CV^{-1} m^{-1}
ζ	=	wall zeta potential, V
ζ^*	=	dimensionless wall zeta potential
θ	=	dimensionless temperature, Eq. (14)
K	=	dimensionless Debye–Huckel parameter, H/λ_D
λ_D	=	Debye length, m
μ	=	dynamic viscosity, kgm^{-1} s^{-1}
ρ	=	density, kgm^{-1}
ρ_e	=	net electric charge density, Cm^{-3}
σ	=	liquid electrical resistivity, Ωm
$\boldsymbol{\tau}$	=	stress tensor, Pa
τ_{xy}	=	shear stress, Pa
Φ	=	externally imposed electrostatic potential, V
φ	=	electrostatic potential, V
ψ	=	electric double-layer potential, V
ψ^*	=	dimensionless electric double-layer potential, $ez\psi/k_B T_{\mathrm{av}}$

Subscripts

av	=	average
m	=	mean

Received 11 October 2010; revision received 29 January 2011; accepted for publication 12 February 2011.

*Ph.D. Student, School of Mechanical Engineering, P.O. Box 11155-9567; armansadeghi@mech.sharif.edu.

†M.Sc. Graduate, School of Mechanical Engineering, P.O. Box 11155-9567; hadiyavari.ir@gmail.com.

‡Professor, School of Mechanical Engineering, P.O. Box 11155-9567; saman@sharif.edu.

§Professor, Department of Mechanical Engineering; suman@mech.iitkgp.ernet.in.

w = wall
0 = neutral liquid

Superscript

g = guess value

I. Introduction

HAVING been explored about two centuries ago [1], electroosmosis now has many applications in fluid delivery at microscale, sample collection, detection, mixing, and separation of various biological and chemical species. Electroosmosis refers to liquid flow induced by an electric field along electrostatically charged surfaces. The electric field may be the result of external or flow-induced potentials. Generally, most substances will acquire a surface electric charge when brought into contact with an aqueous medium. The effect of any charged surface in an electrolyte solution will be to influence the distribution of nearby ions in the solution, and the outcome is the formation of an electric double layer (EDL). The electric double layer, which is shown in Fig. 1, is a region close to the charged surface in which there is an excess of counterions over coions to neutralize the surface charge. The counterions will therefore predominate in EDL, so application of an external electric field results in a net migration of ions in the surface liquid layer. Because of viscous drag, the liquid is drawn by the ions and therefore flows through the channel. The flow rate induced by electroosmosis is usually small, and therefore its applications are limited to the microscale.

Electrokinetic flow in ultrafine capillary slits was first analyzed by Burgreen and Nakache [2]. Rice and Whitehead [3] investigated fully developed electroosmotic flow in a narrow cylindrical capillary for low zeta potentials, using the Debye–Huckel linearization. Levine et al. [4] extended Rice and Whitehead's [3] work to high zeta potentials by means of an approximation method. More recently, an analytical solution for electroosmotic flow in a cylindrical capillary was derived by Kang et al. [5] by solving the complete Poisson–Boltzmann equation for arbitrary zeta potentials. They [6] also analytically analyzed electroosmotic flow through an annulus under the situation when the two cylindrical walls carry high zeta potentials. Hydrodynamic characteristics of the fully developed electroosmotic flow in a rectangular microchannel were reported in a numerical study by Arulanandam and Li [7]. Xuan and Li [8] developed general solutions for electrokinetic flow in microchannels with arbitrary geometry and arbitrary distribution of wall charge. Electroosmotic flow in parallel-plate microchannels for the cases in which electric double layers interact with each other was analyzed by Talapatra and Chakraborty [9,10].

Unlike hydrodynamic features, the study of thermal features of electroosmosis is recent. Maynes and Webb [11] were the first who considered the thermal aspects of the electroosmotic flow due to an external electric field. They analytically studied fully developed, electroosmotically generated, convective transport for a parallel-plate microchannel and circular microtube under imposed boundary conditions of constant wall heat flux and constant wall temperature. Liechty et al. [12] extended the above work to high zeta potentials. It was determined that elevated values of wall zeta potential produce significant changes in the charge potential, electroosmotic flowfield, temperature profile, and Nusselt number relative to previous results invoking the Debye–Huckel linearization. Thermally developing electroosmotically generated flows in circular and rectangular microchannels have been considered by Broderick et al. [13] and Iverson et al. [14], respectively.

Despite various advantages of electroosmotic pumping systems, the Joule heating, which arises due to the applied electric field and the resistivity of the fluid, is an unfavorable phenomenon. The temperature rise due to the Joule heating might be detrimental for handling thermally labile biological samples [15]. Therefore, a pressure-driven pumping system is sometimes added to the electroosmotic pumping systems in order to reduce the Joule heating effects, resulting in a combined electroosmotically and pressure-driven pumping. Such a combined flow may also arise when an electrolyte is driven by means of a pressure gradient through a channel with charged walls. In this situation, an electric potential called the flow-induced potential is created as a result of the accumulation of counterions by the flow in the downstream. The flow-induced potential causes moving the charges and molecules in the opposite direction of the flow, creating extra impedance to the flow motion.

Mala et al. [16] analyzed the flow characteristics of water through a microchannel between two parallel plates with electrokinetic effects. Yang et al. [17,18] studied the effects of the electric double layer near the solid–liquid interface and the flow-induced electrokinetic field on the pressure-driven flow and heat transfer through a rectangular microchannel. Chakraborty [19] obtained analytical solutions of Nusselt number for thermally fully developed flow in microtubes under a combined action of electroosmotic forces and imposed pressure gradients. Das and Chakraborty [20] studied the effect of ionic conductivity variations within the electric double layer on the streaming potential estimation in pressure-driven fluidic transport through narrow confinements.

Some phenomena that are not usually significant at macroscale may become important at microscale. One of these phenomena is viscous dissipation, which may become important because of small dimensions. The effect of viscous dissipation in fully developed electroosmotic heat transfer for a parallel-plate microchannel and circular microtube under imposed boundary conditions of constant wall heat flux and constant wall temperature was analyzed by Maynes and Webb [21].They concluded that the influence of viscous dissipation is only important at low values of the dimensionless Debye–Huckel parameter. Sadeghi and Saidi [22] derived analytical solutions for thermal features of combined electroosmotically and pressure-driven flow in a slit microchannel, by taking into account the effects of viscous heating. Sharma and Chakraborty [15] have obtained semi-analytical solutions for the temperature and Nusselt number distribution in the thermal entrance region of parallel-plate microchannels under the combined action of pressure-driven and electroosmotic transport mechanisms in the presence of viscous dissipation.

The majority of the above-mentioned papers consider a number of assumptions in their analysis. These assumptions mainly include the validity of the Debye–Huckel linearization, uniformity of the Joule heating distribution, and negligibility of viscous heating and

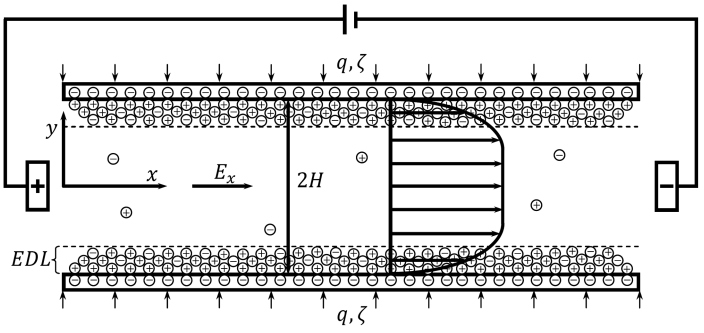

Fig. 1 Geometry of the physical problem, coordinate system, and electric double layer.

variations of the thermophysical properties. It is not clearly known how one of these assumptions is valid for practical applications when the others are not and what its range of applicability is. For example, it is suspected that the assumption of a constant viscosity can become invalid when the viscous dissipation and Joule heating effects are significant. The effects of viscous heating on the flow characteristics are only known for low amounts of the zeta potential, and the effect of the amount and direction of the pressure gradient on the applicability of the Debye–Huckel linearization has not been already explored. Therefore, there is a need for a comprehensive parametric study that considers the interactive effects of viscous dissipation, Joule heating, and temperature-dependent properties in combined electro-osmotically and pressure-driven flow at high zeta potentials. The present work is a response to the above demand that focuses on a slit microchannel with constant wall heat fluxes. The governing equations of fully developed conditions are first made dimensionless and then converted into appropriate difference equations by means of an implicit finite difference method. The resultant systems of algebraic equations are iteratively solved by the tridiagonal matrix algorithm (TDMA) solver. Afterward, an analysis is performed to determine the practical ranges of the flow parameters; finally, the results are presented based on the practical values of the flow parameters.

II. Problem Formulation

The fully developed combined electroosmotically and pressure-driven flow in a slit microchannel with channel half-height of H is considered. The flow geometry is illustrated in Fig. 1. It is assumed that the channel walls are subject to constant values of the heat flux and zeta potential. With the exceptions of the fluid viscosity and electrical resistivity, the thermophysical properties are considered to be constant. This is due to the fact that the variations of the other properties with the temperature are not significant. For water, increasing the temperature from 20 to 70°C leads to approximately 59% variation in both the viscosity and electrical resistivity [23,24]. However, the corresponding variations for the density, thermal conductivity, and fluid permittivity are 2, 10, and 20%, respectively [23,24]. Therefore, by calculating the latter properties at the mean temperature, their overall variations become less than 10%, which seems to be insignificant. It is also assumed that the liquid contains an ideal solution of fully dissociated symmetric salt and the charge in the EDL follows Boltzmann distribution.

A. Governing Equations

The electrical potential distribution is obtained from solution of the Poisson equation:

$$\nabla^2\varphi = -\frac{\rho_e}{\varepsilon} \tag{1}$$

where ε is the fluid permittivity, and ρ_e is the net electric charge density. The potential φ is due to combination of externally imposed field Φ and EDL potential ψ: namely,

$$\varphi = \Phi + \psi \tag{2}$$

For an ideal solution of fully dissociated symmetric salt, the electric charge density is given by [25]

$$\rho_e = -2n_0 ez \sinh\left(\frac{ez\psi}{k_B T}\right) \tag{3}$$

where n_0 is the ion density, e is the proton charge, z is the valence number of ions in solution, k_B is the Boltzmann constant, and T is the absolute temperature. For fully developed flow, $\psi = \psi(y)$ and the external potential gradient is in the axial direction only, i.e., $\Phi = \Phi(x)$. For a constant voltage gradient in the x direction, Eq. (1) becomes

$$\frac{\mathrm{d}^2\psi}{\mathrm{d}y^2} = \frac{2n_0 ez}{\varepsilon}\sinh\left(\frac{ez\psi}{k_B T}\right) \tag{4}$$

The above nonlinear second-order one-dimensional equation is known as the Poisson–Boltzmann equation. Yang et al. [18] have shown with extensive numerical simulations that the effect of temperature on the potential distribution is negligible. Therefore, the potential field and the charge density may be calculated on the basis of an average temperature T_{av}. Using this assumption, Eq. (4) in the dimensionless form becomes

$$\frac{\mathrm{d}^2\psi^*}{\mathrm{d}y^{*2}} = \frac{2n_0 e^2 z^2}{\varepsilon k_B T_{\mathrm{av}}} H^2 \sinh\psi^* \tag{5}$$

where $\psi^* = ez\psi/k_B T_{\mathrm{av}}$ and $y^* = y/H$. The quantity $(2n_0 e^2 z^2/\varepsilon k_B T_{\mathrm{av}})^{-1/2}$ is known as Debye length, λ_D. Defining the dimensionless Debye–Huckel parameter as $K = H/\lambda_D$, we come up with

$$\frac{\mathrm{d}^2\psi^*}{\mathrm{d}y^{*2}} - K^2 \sinh\psi^* = 0 \tag{6}$$

The boundary conditions for the above equation are

$$\psi^*_{(1)} = \zeta^*, \qquad \left(\frac{\mathrm{d}\psi^*}{\mathrm{d}y^*}\right)_{(0)} = 0 \tag{7}$$

where ζ^* is the dimensionless wall zeta potential, i.e., $\zeta^* = ez\zeta/k_B T_{\mathrm{av}}$. Although an analytical solution of Eq. (6) in terms of the first kind elliptic integral exists [2], because of its difficulty to use, Eq. (6) subject to the above boundary conditions is solved numerically.

The momentum exchange through the flowfield is governed by the Cauchy equation:

$$\rho\frac{\mathrm{D}\mathbf{u}}{\mathrm{D}t} = -\nabla p + \nabla\cdot\boldsymbol{\tau} + \mathbf{F} \tag{8}$$

where ρ denotes the density, p represents the pressure, $\mathbf{u}$ and $\mathbf{F}$ are the velocity and body force vectors, respectively, and $\boldsymbol{\tau}$ is the stress tensor. Here, the body force acts in the x direction and equals $\rho_e E_x$, with $E_x = -\mathrm{d}\Phi/\mathrm{d}x$ denoting the electric field. Regarding that $\mathrm{D}\mathbf{u}/\mathrm{D}t = 0$ at fully developed conditions, we come up with the following expression for the momentum equation in the x direction:

$$\frac{\partial}{\partial y}\left(\mu(T)\frac{\mathrm{d}u}{\mathrm{d}y}\right) = \frac{\mathrm{d}p}{\mathrm{d}x} + 2E_x n_0 ez \sinh\left(\frac{ez\psi}{k_B T_{\mathrm{av}}}\right) \tag{9}$$

The relevant boundary conditions for the momentum equation are the symmetry condition at centerline and no slip condition at the wall.

The conservation of energy including the effects of viscous dissipation and Joule heating provides

$$\rho c_p \frac{\mathrm{D}T}{\mathrm{D}t} = \nabla\cdot(k\nabla T) + \nabla\mathbf{u}\colon\boldsymbol{\tau} + s \tag{10}$$

In the above equation, s and $\nabla\mathbf{u}\colon\boldsymbol{\tau}$ denote the rate of volumetric heat generation due to Joule heating and viscous dissipation, respectively. The Joule heating term equals $s = E_x^2/\sigma(T)$, where $\sigma(T)$ is the liquid electrical resistivity given by [4]

$$\sigma(T) = \frac{\sigma_0(T)}{\cosh(ez\psi/k_B T_{\mathrm{av}})} \tag{11}$$

where $\sigma_0(T)$ is the electrical resistivity of the neutral liquid. The hyperbolic term in the above equation accounts for the fact that the resistivity within the EDL is lower than that of the neutral liquid, due to an excess of ions close to the surface. For steady fully developed flow, $\mathrm{D}T/\mathrm{D}t = u(\partial T/\partial x)$ and $\nabla\mathbf{u}\colon\boldsymbol{\tau} = \tau_{xy}(\mathrm{d}u/\mathrm{d}y) = \mu(T)(\mathrm{d}u/\mathrm{d}y)^2$, so the energy equation (10) becomes

$$\rho c_p u\frac{\partial T}{\partial x} = k\left(\frac{\partial^2 T}{\partial x^2} + \frac{\partial^2 T}{\partial y^2}\right) + \mu(T)\left(\frac{\mathrm{d}u}{\mathrm{d}y}\right)^2 + \frac{E_x^2}{\sigma_0(T)}\cosh\left(\frac{ez\psi}{k_B T_{\mathrm{av}}}\right) \tag{12}$$

The energy equation is constrained by the following boundary conditions:

$$\left(\frac{\partial T}{\partial y}\right)_{(x,0)} = 0 \qquad T_{(x,H)} = T_w(x) \quad \text{and} \quad k\left(\frac{\partial T}{\partial y}\right)_{(x,H)} = q \tag{13}$$

The usual way of modeling the thermally fully developed flow is to define the following dimensionless temperature, which is independent of the axial direction:

$$\theta(y) = \frac{T - T_w}{qH/k} \tag{14}$$

Taking differentiation of Eq. (14) with respect to x gives

$$\frac{\partial T}{\partial x} = \frac{\mathrm{d}T_w}{\mathrm{d}x} = \frac{\mathrm{d}T_m}{\mathrm{d}x} \tag{15}$$

where T_m is the mean temperature. From an energy balance on a length of duct dx, the following expression is obtained for $\mathrm{d}T_m/\mathrm{d}x$:

$$\frac{\mathrm{d}T_m}{\mathrm{d}x} = \frac{q + \int_0^H [\mu(T)(\frac{\mathrm{d}u}{\mathrm{d}y})^2 + \frac{E_x^2}{\sigma_0(T)}\cosh(\frac{ez\psi}{k_B T_{\mathrm{av}}})]\,\mathrm{d}y}{\rho c_p u_m H} \tag{16}$$

where u_m is the mean velocity. If we were dealing with the constant-properties case, the above expression for $\mathrm{d}T_m/\mathrm{d}x$ would be independent of the axial coordinate and, as a result, the axial conduction term in the energy equation would vanish. It is still possible to make an order-of-magnitude analysis in order to determine whether or not the axial conduction term may be neglected in favor of the other terms. For this reason, the temperature dependencies of the viscosity and electrical resistivity should be known. Here, the variation of the viscosity with temperature is assumed to be in the following form [26]:

$$\mu = \mu_w e^{-\gamma(T-T_w)} \tag{17}$$

where $\mu_w = \mu_w(x)$ is the viscosity of the fluid at the wall. For the liquid electrical resistivity, the following temperature dependency is considered [27]:

$$\sigma_0 = \frac{\sigma_{0,w}}{1 + \beta(T - T_w)} \tag{18}$$

where $\sigma_{0,w} = \sigma_{0,w}(x)$ is the liquid electrical resistivity at the wall. Regarding Eqs. (12), (15), and (16), the ratio of the energy transferred by conduction to the energy transferred by the mechanism of convection in the axial direction will be

$$\frac{k\mathrm{d}^2T_w/\mathrm{d}x^2}{\rho c_p u \mathrm{d}T_w/\mathrm{d}x} = \frac{k}{\rho^2 c_p^2 u u_m H \mathrm{d}T_w/\mathrm{d}x} \times \int_0^H \left[\frac{\partial \mu(T)}{\partial x}\left(\frac{\mathrm{d}u}{\mathrm{d}y}\right)^2 - \frac{E_x^2}{\sigma_0^2(T)}\frac{\partial \sigma_0(T)}{\partial x}\cosh\left(\frac{ez\psi}{k_B T_{\mathrm{av}}}\right)\right]\mathrm{d}y \tag{19}$$

Using Eqs. (15), (17), and (18), the terms $\partial\mu(T)/\partial x$ and $\partial\sigma_0(T)/\partial x$ may be evaluated as

$$\frac{\partial \mu(T)}{\partial x} = \frac{\mathrm{d}\mu_w}{\mathrm{d}x}e^{-\gamma(T-T_w)} = \frac{\mathrm{d}\mu_w}{\mathrm{d}T_w}\frac{\mathrm{d}T_w}{\mathrm{d}x}e^{-\gamma(T-T_w)} = -\gamma\mu_w\frac{\mathrm{d}T_w}{\mathrm{d}x}e^{-\gamma(T-T_w)} \tag{20}$$

$$\frac{\partial \sigma_0(T)}{\partial x} = \frac{\frac{\mathrm{d}\sigma_{0,w}}{\mathrm{d}x}}{1 + \beta(T - T_w)} = \frac{(\mathrm{d}\sigma_{0,w}/\mathrm{d}T_w)\mathrm{d}T_w/\mathrm{d}x}{1 + \beta(T - T_w)} = -\frac{\mathrm{d}T_w}{\mathrm{d}x}\frac{\beta\sigma_{0,w}}{1 + \beta(T - T_w)} \tag{21}$$

Therefore, Eq. (19) becomes

$$\frac{k\mathrm{d}^2T_w/\mathrm{d}x^2}{\rho c_p u \mathrm{d}T_w/\mathrm{d}x} = \frac{k\beta E_x^2}{\rho^2 c_p^2 u u_m H \sigma_{0,w}} \times \int_0^H \left\{[1 + \beta(T - T_w)]\cosh\left(\frac{ez\psi}{k_B T_{\mathrm{av}}}\right)\right\}\mathrm{d}y - \frac{k\gamma\mu_w}{\rho^2 c_p^2 u u_m H}\int_0^H e^{-\gamma(T-T_w)}\left(\frac{\mathrm{d}u}{\mathrm{d}y}\right)^2\mathrm{d}y \tag{22}$$

The electric field is of the order $\mu_w u_m/\varepsilon\zeta$, and for a usual value of the zeta potential the first integral will be of the order H. Therefore, the first term is of the order $k\beta\mu_w^2/\rho^2 c_p^2 \varepsilon^2\zeta^2\sigma_{0,w}$. Two limiting cases should be considered in evaluating the second term. For convenience, let us assume a purely electroosmotic flow. For low values of the dimensionless Debye–Huckel parameter, large velocity gradients do not exist. So the velocity gradient may be scaled based on the mean velocity and the channel half-height. For high values of K, the velocity over much of the channel cross section is uniform with essentially no velocity gradient, and a large velocity gradient exists near the wall. In this case, the length over which a velocity gradient exists, δ, is of the same order as the Debye length, λ_D. Therefore, for high values of K, the second integral is of the order u_m^2/λ_D, while for low values of K, it is of the order u_m^2/H. Ultimately, the second term for low and high values of K is of the order $k\gamma\mu_w/\rho^2 c_p^2 H^2$ and $k\gamma\mu_w/\rho^2 c_p^2 H\lambda_D$, respectively. Let us consider water as the working fluid moving in a channel with channel half-height of 1 μm. At 25°C and for the minimum value of the Debye length, which is about 1 nm, the second term is approximately 5.65×10^{-4} for high values of K, while for low values of K it is about 5.65×10^{-7}. Assuming the values of 25 mV and 1000 Ωm, respectively, for the zeta potential and the electrical resistivity, the first term will approximately be 0.0023. Therefore, the ratio of the diffused energy to the energy transferred by the flow is, at most, about 0.0023, which means that for most practical applications, the axial conduction term may be discarded from the energy equation in favor of the other terms.

By considering the temperature dependencies of the viscosity and electrical resistivity from Eqs. (17) and (18), respectively, and taking advantage of Eq. (16), the dimensionless forms of the momentum and energy equations become

$$e^{-\frac{AK^2\theta}{S}}\left(\frac{\partial^2 u^*}{\partial y^{*2}} - \frac{AK^2}{S}\frac{\mathrm{d}\theta}{\mathrm{d}y}\frac{\partial u^*}{\partial y^*}\right) = -2\Gamma - \frac{K^2}{\zeta^*}\sinh\psi^* \tag{23}$$

$$\frac{\mathrm{d}^2\theta}{\mathrm{d}y^{*2}} = \left(1 + I_1 S + I_2\frac{SS_v}{K^2}\right)\frac{u^*}{u_m^*} - \frac{SS_v}{K^2}e^{-\frac{AK^2\theta}{S}}\left(\frac{\partial u^*}{\partial y^*}\right)^2 - S\left(1 + \frac{BK^2\theta}{S}\right)\cosh\psi^* \tag{24}$$

where Γ is the ratio of the pressure-driven velocity scale to the Helmholtz–Smoluchowski electroosmotic velocity: namely, $\Gamma = u_{\mathrm{PD}}/u_{\mathrm{HS}}$, where $u_{\mathrm{PD}} = -H^2(\mathrm{d}p/\mathrm{d}x)/2\mu_w$ and $u_{\mathrm{HS}} = -\varepsilon\zeta E_x/\mu_w$. The other dimensionless variables are given below:

$$A = \frac{\gamma\lambda_D^2 E_x^2}{k\sigma_{0,w}}, \qquad B = \frac{\beta\lambda_D^2 E_x^2}{k\sigma_{0,w}}, \qquad u^* = \frac{u}{u_{\mathrm{HS}}}$$
$$S_v = \frac{\mu_w\sigma_{0,w}u_{\mathrm{HS}}^2}{E_x^2\lambda_D^2}, \qquad S = \frac{E_x^2 H}{q\sigma_{0,w}}, \qquad u_m^* = \int_0^1 u^*\,\mathrm{d}y^*$$
$$I_1 = \int_0^1\left(1 + \frac{BK^2\theta}{S}\right)\cosh\psi^*\,\mathrm{d}y^*$$
$$I_2 = \int_0^1 e^{-\frac{AK^2\theta}{S}}\left(\frac{\partial u^*}{\partial y^*}\right)^2\mathrm{d}y^* \tag{25}$$

The corresponding nondimensional boundary conditions for the momentum and energy equations are

$$\left.\frac{\partial u^*}{\partial y^*}\right|_{y^*=0}=0, \qquad u^*|_{y^*=1}=0 \tag{26}$$

$$\left.\frac{\mathrm{d}\theta}{\mathrm{d}y^*}\right|_{y^*=0}=0, \qquad \theta|_{y^*=1}=0 \tag{27}$$

As it is clear from Eqs. (23) and (24), the velocity and temperature fields are coupled through the property dependence on temperature, and thus the governing equations together with the boundary conditions (26) and (27) should be solved simultaneously by means of a numerical method.

B. Friction Factor and Nusselt Number

Once the velocity and temperature fields have been obtained, the parameters of physical interest can be calculated. One of the important parameters of the hydrodynamics is the friction factor defined as

$$f=\frac{2\tau_{xy,w}}{\rho u_m^2} \tag{28}$$

where $\tau_{xy,w}$ is the wall shear stress. The final form of the friction factor in the form of the Poiseuille number is

$$fRe=-8\frac{\partial u^*/\partial y^*|_{y^*=1}}{u_m^*} \tag{29}$$

where $Re=\rho u_m D_h/\mu_w$, and $D_h=4H$ is the channel hydraulic diameter.

The heat transfer rates are expressed in the form of the Nusselt number. To calculate the Nusselt number, first the dimensionless mean temperature should be obtained. The dimensionless mean temperature is written as

$$\theta_m=\frac{\int_0^1 u^*\theta\,\mathrm{d}y^*}{\int_0^1 u^*\,\mathrm{d}y^*}=\frac{\int_0^1 u^*\theta\,\mathrm{d}y^*}{u_m^*} \tag{30}$$

Based on the definition, the Nusselt number is written as

$$Nu=\frac{hD_h}{k}=\frac{qD_h}{k(T_w-T_m)}=-\frac{4}{\theta_m} \tag{31}$$

C. Numerical Method

An implicit finite difference method for a uniform grid is used to solve the dimensionless forms of the governing equations. By means of the central difference scheme, Eqs. (6), (23), and (24), for the inner points are converted into the following difference equations:

$$\psi_{i+1}^*-[2+K^2(\Delta y^*)^2\Lambda_i^g]\psi_i^*+\psi_{i-1}^*=0 \tag{32}$$

$$\begin{aligned}&\left[1-\frac{AK^2}{4S}(\theta_{i+1}^g-\theta_{i-1}^g)\right]u_{i+1}^*-2u_i^*\\&\quad+\left[1+\frac{AK^2}{4S}(\theta_{i+1}^g-\theta_{i-1}^g)\right]u_{i-1}^*\\&\quad=-(\Delta y^*)^2e^{\frac{AK^2}{S}\theta_i^g}\left(2\Gamma+\frac{K^2}{\zeta^*}\sinh\psi_i^*\right)\end{aligned} \tag{33}$$

$$\begin{aligned}&\theta_{i+1}-[2(\Delta y^*)^2BK^2\cosh\psi_i^*]\theta_i+\theta_{i-1}\\&\quad=(\Delta y^*)^2\left(1+I_1^gS+I_2^g\frac{SS_v}{K^2}\right)\frac{u_i^{*g}}{u_m^{*g}}\\&\quad-\frac{SS_v}{4K^2}e^{-\frac{AK^2}{S}\theta_i^g}(u_{i+1}^{*g}-u_{i-1}^{*g})^2-S(\Delta y^*)^2\cosh\psi_i^*\end{aligned} \tag{34}$$

Here, the superscript g denotes the guess values and the parameter $\Lambda_i=\sinh\psi_i^*/\psi_i^*$ is used to supply a better convergence, since treating the term $\sinh\psi_i^*$ in Eq. (6) as a source term led to the instability of the solution. For the grid point located on the symmetry boundary, appropriate difference equations are used. The solution procedure starts by guessing the appropriate distributions for the potential, velocity, and temperature fields. Once the potential distribution is obtained, the values of I_1, I_2, and u_m^* are evaluated by means of the Cavalieri–Simpson method for integration. Afterward, the resultant systems of algebraic equations are iteratively solved by the TDMA solver to determine the new values of the velocity and temperature at each grid point. The solution procedure is going on until the convergence criterion is satisfied. Here, the appropriate value of the convergence criterion, chosen as the maximum relative difference of the flow parameters in two successive iterations through the flow domain, is found to be 10^{-8}.

III. Method Validation

It is convenient to initially perform a grid dependency analysis to determine the appropriate number of grid points that provides reliable results. The appropriate number of grid points evidently increases with increasing the dimensionless Debye–Huckel parameter and the dimensionless zeta potential, since at higher values of K and ζ^* finer meshes are needed to capture the huge gradients near the wall.

Figure 2 shows the grid dependency of the Nusselt number values for $\zeta^*=5$. For low K and ζ^*, accurate predictions may be achieved with a few hundreds of grid points while at the extreme values of both K and ζ^*, obtaining accurate results may require several ten thousands of grid points. For $K\le 100$, the results obtained by means of 1000 and 5000 grid points are sufficiently accurate for $\zeta^*=1$ and 5, respectively. Therefore, for reduction of computational costs, in graph generation, $1000\zeta^*$ grid points are used for $K\le 100$, and for higher values of the dimensionless Debye–Huckel parameter, we set $n=10K\zeta^*$, with n being the number of grid points.

After the grid dependency, a comparison with existing literature data is needed to validate the accuracy of the developed code. The analytical solution given by Sadeghi and Saidi [22] is chosen for comparison. This solution is related to constant fluid properties and assumes uniform distribution of Joule heating and applicability of the Debye–Huckel linearization, i.e., $\sinh\psi^*\cong\psi^*$. For this reason, $\sinh\psi_i^*$ and $\cosh\psi_i^*$ in Eqs. (32–34) are, respectively, replaced with ψ_i^* and 1. Furthermore, the terms containing A and B are removed from Eqs. (33) and (34). It is noteworthy that Sadeghi and Saidi [22] have used the Brinkman number, $Br=SS_v u_m^{*2}/K^2$, to characterize the effects of viscous heating. Table 1 compares the present results against those predicted by the aforementioned expression and reveals an excellent agreement between the results.

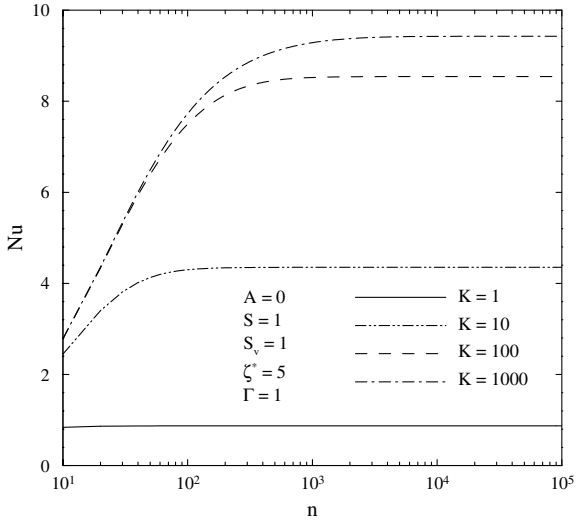

Fig. 2 Grid dependency of the Nusselt number values.

Table 1 Comparison of Nusselt number values for purely electroosmotic flow with constant fluid properties at $S = -0.5$

	$S_v = 1$		$S_v = 10$	
K	Present study	Sadeghi and Saidi [22]	Present study	Sadeghi and Saidi [22]
1	9.5970	9.5969	18.8444	18.8430
10	10.9104	10.9104	13.7964	13.7963
100	11.8549	11.8549	12.1257	12.1257
1000	11.9851	11.9851	12.0121	12.0121

IV. Practical Ranges of the Flow Parameters

Since we aim at studying the practical applications, it is vital to estimate the realistic ranges of the flow parameters. On this basis, attention should be given to the fact that actually electroosmotic flows are not typically used for heat sink purpose, because of Joule heating involved. These kinds of problems are more relevant in biotechnology applications in which all, or a considerable amount of, the energy generated by internal heating is dissipated through the walls, giving a negative wall heat flux. Therefore, the flow parameters have the same order of those pertinent to the case that all the internal heating is dissipated through the walls, yielding $\partial T/\partial x = 0$. It is noteworthy that although this case yields a constant value for the wall temperature, it is nevertheless a case of constant wall heat flux as well and may be studied by the method presented here. For this case, the minimum value of $|S|$ corresponds to the situation that highest amounts of viscous heating and the parameter I_1 exist. As has been shown by Maynes and Webb [21], for purely electroosmotic flow, the amount of internal heating due to viscous dissipation is more significant at low values of K and may reach as twice as Joule heating for practical applications. Maximum value of I_1 corresponds to the highest zeta potential along with lowest K and it is about 12 for $\zeta^* = 5$ and $K = 1$. Therefore, lowest amount of $|S|$ may theoretically be close to zero for a low value of K. The highest theoretical value of $|S|$ is infinity, which corresponds to the situation that the walls are insulated and all the internal heating is convected downstream by the flow. We assume that the wall heat flux is always comparable with the internal heating and thus restrict $|S|$ to 5 in the present study.

By substitution of the Helmholtz–Smoluchowski velocity from its definition, the viscous heating parameter may be written based on more fundamental parameters as $S_v = \sigma_{0,w}\varepsilon^2\zeta^2/\mu_w\lambda_D^2$. S_v is therefore dependent only on physical and electroosmotic properties of the liquid. As stated by Maynes and Webb [21], for practical applications, S_v may be assumed to have maximum values of the order of 10.

The viscosity variation parameter A for a particular fluid is evidently dependent on the Debye length and the strength of the electric field. Therefore, the maximum amount of A corresponds to the maximum practical values of the electric field and the Debye length, which are 100 kVm^{-1} and 500 nm, respectively [21,28]. So for water with $\sigma_{0,w} = 100\ \Omega\text{m}$, the maximum amount of the viscosity variation parameter will be about 7×10^{-7}. Here, we assume a maximum value of 1×10^{-6} for the viscosity variation parameter. It should be pointed out that when using the maximum amount of A, the dimensionless Debye–Huckel parameter is limited to about 300, since the maximum practical value of the channel half-height is about 150 μm [28]. Table 2 indicates the practical ranges of the problem parameters obtained in the present study or taken from Karniadakis et al. [28] and Maynes and Webb [21]. It should be pointed out that, assuming a univalent solution at 25°C, the zeta potential range presented in the table will result in values of below 4 for $|\zeta^*|$.

Table 2 Practical ranges of the problem parameters obtained in the present study or taken from Karniadakis et al. [28] and Maynes and Webb [21]

Parameter	Value
Half channel height H	0.005–150 μm
Debye length λ_D	1–500 nm
Zeta potential ζ	$\pm$1– $\pm$ 100 mV
Electric field E_x	1–100 kVm^{-1}
Viscosity variation parameter A	$<10^{-6}$
Viscous heating parameter S_v	≤ 10
Dimensionless Joule heating parameter S	<0

V. Results and Discussion

Regarding numerous flow parameters, it is impossible to study all aspects of the flow in the present work. Thus, it is assumed that the working fluid is water, for which $\beta \cong 1.4\gamma$ [24]. As a result, we can set $B = 1.4A$ to decrease the number of flow parameters. First of all, let us consider the potential distribution, which is shown in Figs. 3 and 4. Note that the simplified case is that obtained by the Debye–Huckel linearization [22]. In the literature, it is well known that the Debye–Huckel linearization is valid for $\zeta^* \leq 1$. Figure 3 demonstrates that performing this linearization does not lead to significant error up to $\zeta^* \cong 2$, which corresponds to the value of about 51.4 mV for the zeta potential at standard conditions. According to Karniadakis et al. [28], the zeta potential range for practical applications is 1–100 mV, implying that the Debye–Huckel linearization may successfully be used to more than half of the practical applications range of the zeta potential. Figure 4 exhibits that this linearization may be used even for higher zeta potentials if a sufficiently high value of K is considered. This is due to the fact that at higher amounts of K, the dimensionless potential is lower than 1 over much of the duct cross section. As observed, $K = 100$ may be used as the criterion for using the Debye–Huckel linearization at $\zeta^* = 5$ and, consequently, for the majority of the practical applications.

The transverse distribution of the dimensionless velocity at different values of Γ and ζ^* is depicted in Fig. 5. The results obtained by means of the Debye–Huckel linearization are denoted by dashed lines. When using this linearization, the dimensionless velocity is not dependent on the dimensionless wall zeta potential. As observed, the velocity profiles obtained using the Debye–Huckel linearization are

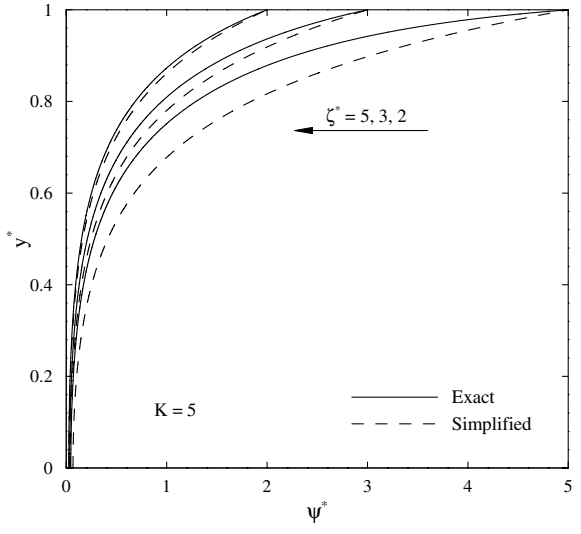

Fig. 3 Transverse distribution of ψ^* at different values of ζ^*.

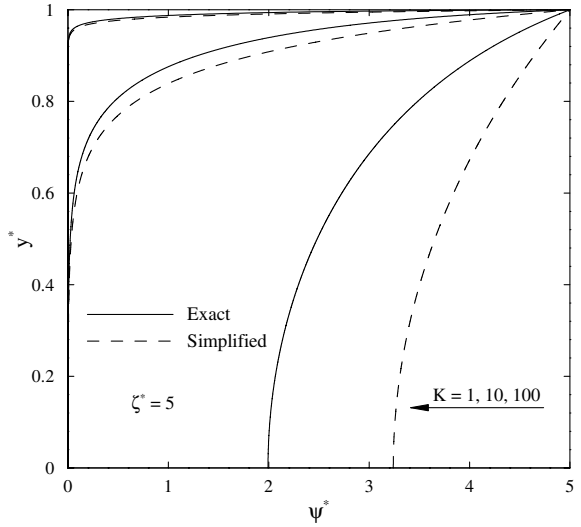

Fig. 4 Transverse distribution of ψ^* at different values of K.

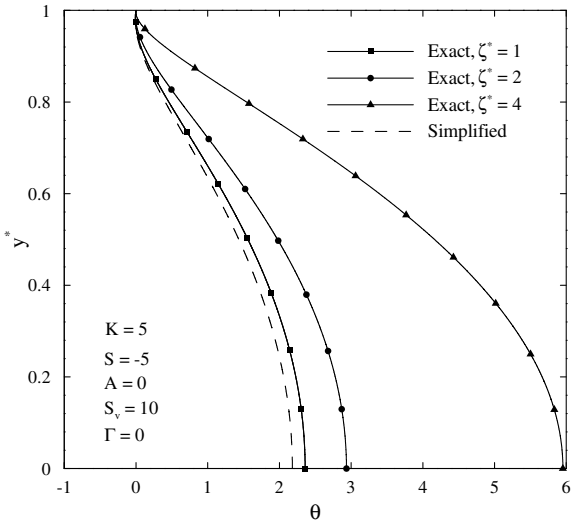

Fig. 6 Transverse distribution of dimensionless temperature at different values of ζ^*.

sufficiently accurate for $\zeta^* = 2$. Therefore, if the aim is to obtain the velocity distribution, this linearization may successfully be used up to $\zeta = 51.4$ mV. The accuracy of the simplified results is higher for the pressure-assisted flow, characterized by $\Gamma = 0.5$, whereas for pressure-opposed flow the discrepancy between the exact and the simplified results becomes more important. Therefore, special care must be taken when using the Debye–Huckel linearization in the presence of considerable amounts of opposed pressure even for low values of the zeta potential.

A comparison between the temperature profile obtained by means of the Debye–Huckel linearization with assumption of uniform distribution of the Joule heating and the exact ones for different zeta potentials is made in Fig. 6. The comparison reveals errors of about 7.5, 26, and 63%, for $\zeta^* = 1$, 2, and 4, respectively, in predicting the temperature distribution at the centerline using the simplified case. Therefore, the simplified case may be successfully applied to $\zeta^* = 1$, however, it fails to supply a good prediction of the temperature field for higher values of the zeta potential. The origin of the discrepancy mainly comes from the assumption of uniform Joule heating distribution and not the Debye–Huckel linearization, which was found to be accurate up to $\zeta^* = 2$ in evaluating the velocity. Therefore, the simplified case may be applied to higher zeta potentials if a sufficiently low value of S is considered. Figure 7 shows that the simplified case is capable of predicting the temperature distribution for higher zeta potentials if a sufficiently high value of the dimensionless Debye–Huckel parameter is considered. Note that this figure is very instructive. As K increases from 10 to 100, the dimensionless temperature changes it sign from positive to negative. Let us interpret this trend by means of energy balance. At $K = 10$, due to a considerable amount of the Joule heating near the wall, the temperature over the majority of the channel cross section is below the wall temperature. The exception is an infinitesimal region close to the wall in which the fluid particles have higher temperatures than the wall, providing a negative wall heat flux. As the dimensionless Debye–Huckel parameter increases, in the wall vicinity, the velocity and, consequently, the energy transferred by the flow increase. The final outcome is thus to decrease the wall temperature and, consequently, the dimensionless temperature. This trend lasts until the wall temperature falls below the fluid particles temperatures, leading to negative values of dimensionless temperature at $K = 100$.

Figure 8a illustrates the transverse distribution of $\mu/\mu_w = e^{-\frac{AK^2}{S}\theta}$ for $A = 1 \times 10^{-6}$ at different values of the velocity scale ratio. As y^* increases, the viscosity increases due to a decrease in the temperature. As seen, the variation of viscosity for pressure-assisted flow is more pronounced than purely electroosmotic flow, whereas the opposite is true for pressure-opposed flow. However, for all the cases, the overall variations are below 9%. Regarding the fact that $\gamma \cong 0.018$ for water, it follows that the temperature variations are about 5 K, which is much lower than 10 K, the criterion considered

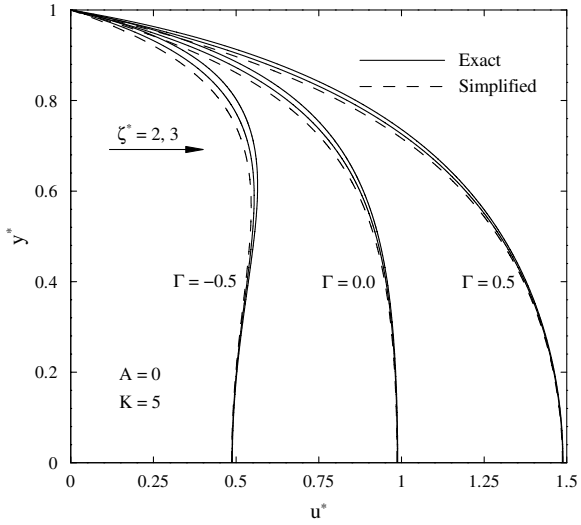

Fig. 5 Transverse distribution of dimensionless velocity at different values of Γ and ζ^*.

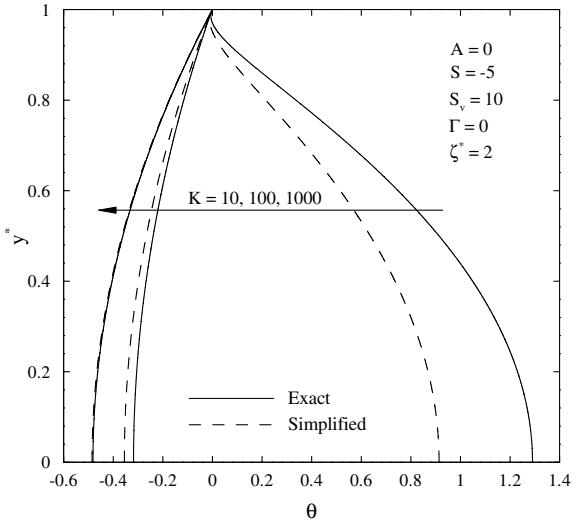

Fig. 7 Transverse distribution of dimensionless temperature at different values of K.

for negligibility of temperature dependency of fluid properties [15]. The smallness of the temperature variations also confirms our assumption in obtaining the potential field and the charge density on the basis of the average temperature. For an average temperature of 300 K, the above temperature variation implies an error of below 1% in evaluating the absolute temperature, which is evidently negligible.

Transverse distributions of the dimensionless velocity and temperature at different values of the velocity scale ratio with and without considering the temperature dependency of the fluid properties are shown in Figs. 8b and 8c, respectively. It can be seen that the effects of variation parameters, i.e., A and B, on the velocity profile for purely electroosmotic flow are negligible. Close to the wall, the viscosity is nearly equal to the reference viscosity and, as a result, the velocity is the same as that obtained by assuming constant fluid properties. As the distance from the wall increases, the viscosity is reduced and the velocity consequently starts to increase. However, this trend ceases to last at a short distance away, at which a sharp decrease occurs in the electrical potential. As known, outside the EDL, at which the body force vanishes, the velocity is not dependent on the viscosity. Therefore, the velocity profile follows that of the constant-properties case with a small margin. Unlike the purely electroosmotic case, the velocity profiles distort in the presence of the pressure gradient. For these cases, the decrease in the viscosity in the bulk region leads to more effects of the pressure gradient and, as a result, the velocity profile moves to the right for pressure-assisted flow and to the left for pressure-opposed flow. The temperature profiles drawn in Fig. 8c reveal that when considering the temperature dependencies of the properties, higher temperature differences between the fluid particles and the wall are obtained. The main origin of this variation comes from the fact that by considering the thermal effects, the energy generated by means of Joule heating increases for the inner points, which have higher temperatures, due to the decrease in the electrical resistivity. It is worth mentioning that although the increase in the Joule heating for these points is accompanied by a decrease in the viscous heating due to viscosity reduction, the effects of Joule heating are dominant for the parameter combination being considered in Fig. 8.

One of the important themes of the present work is to study the effects of viscous dissipation at high zeta potentials. To give a better insight into the effects of viscous heating, it is convenient to initially evaluate the ratio of energy generated by viscous dissipation, E_v, to the energy generated due to Joule heating, E_J, which is given by

$$\frac{E_v}{E_J} = \frac{\mu_w I_2 u_{\mathrm{HS}}^2 / H}{H I_1 E_x^2 / \sigma_{0,w}} = \frac{S_v I_2}{I_1 K^2} \tag{35}$$

The ratio of $E_v/(E_J S_v)$ for different values of Γ is shown in Fig. 9. The figure reveals that for a given S_v, the effect of viscous heating is more pronounced for pressure-assisted flow, whereas its effect is much lower for pressure-opposed flow. This is due to the fact that the favorable pressure gradient increases the mean velocity and, as a result, the velocity gradients, whereas the opposite is true for unfavorable pressure gradient. For all the cases, the maximum values of $E_v/(E_J S_v)$ occur at low amounts of K. Regarding the practical range of the Debye length, which is 1–500 nm, it follows that higher amounts of $E_v/(E_J S_v)$ are related to nanochannels. The figure shows that at high values of S_v, the ratio of viscous heating to the Joule heating in the presence of a considerable amount of favorable pressure gradient may exceed 10 for a nanochannel. At high values of K, the velocity gradient over the majority of the channel cross section is decreased with increasing K. The exception is a region of the order λ_D, in which sharp gradients exist. Increasing K while keeping the dimensionless viscous heating parameter constant means that the Debye length remains unchanged, while the channel height increases. Therefore, the rate of increase in the Joule heating is higher than viscous heating, resulting in lower values of $E_v/(E_J S_v)$, as observed in Fig. 9.

Figure 10 illustrates $E_v/(E_J S_v)$ as a function of K for different values of the dimensionless zeta potential in the absence of pressure gradient. An increase in the zeta potential is accompanied by a decrease in $E_v/(E_J S_v)$ for lower amounts of K, whereas the opposite

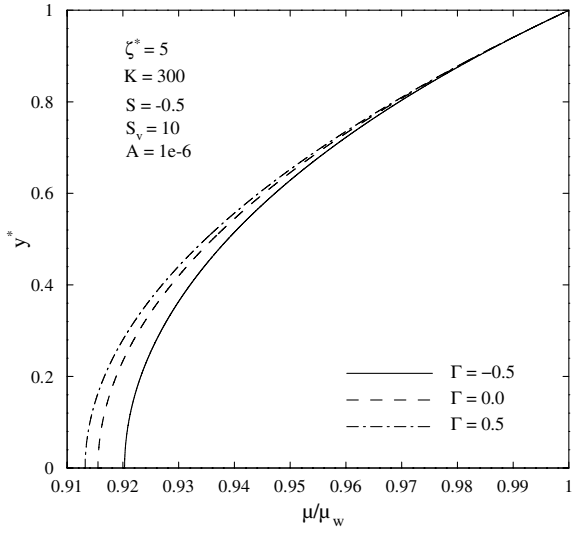

a)

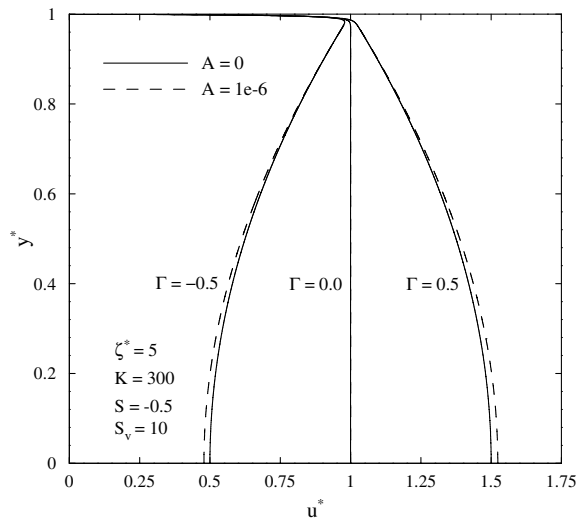

b)

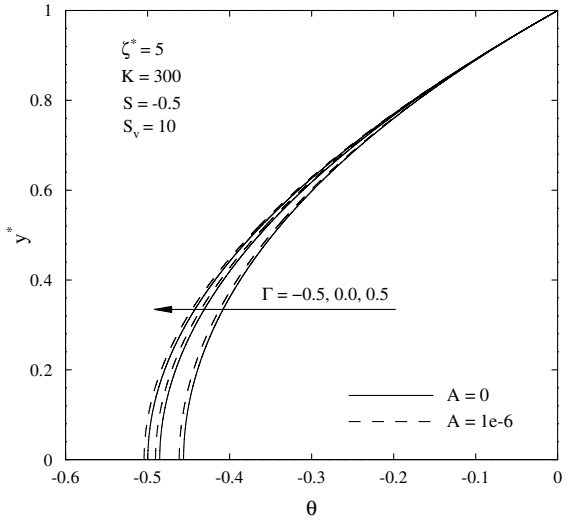

c)

Fig. 8 Transverse distributions of μ/μ_w, u^*, and θ at different values of Γ and A.

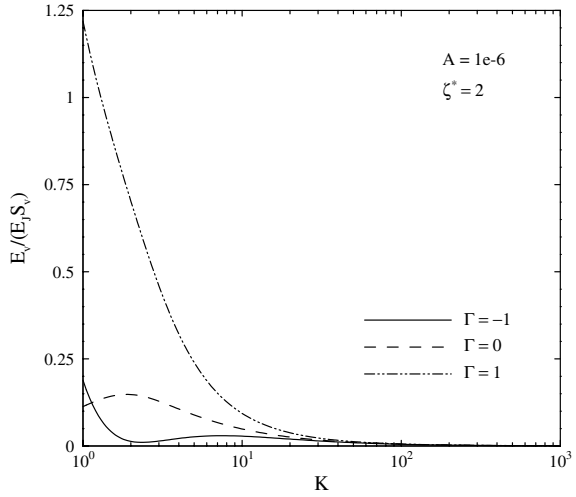

Fig. 9 $E_v/(E_J S_v)$ **as a function of** K **at different values of** Γ **for** $\zeta^* = 2$.

is true for higher values of K. The origin of this behavior comes from the fact that at lower values of K, an increase in the zeta potential leads to a considerable increase in the Joule heating, which overcomes the corresponding increase of viscous heating due to higher velocities. However, at higher values of K, the potential is nearly zero over the majority of the channel cross section. Thus, increasing the zeta potential causes a little increase in the Joule heating, whereas the increase in the viscous heating is still comparable with that for a low value of K. The ultimate outcome is thus an increase in $E_v/(E_J S_v)$.

Poiseuille number and Nusselt number versus dimensionless zeta potential at different values of K for pressure-assisted flow are shown in Fig. 11. Note that by simplified we mean the case that the Debye–Huckel linearization is adopted along with a uniform distribution of the Joule heating. As observed, the exact results reveal that the Poiseuille number is an increasing function of the wall zeta potential. This is in agreement with Fig. 5, which exhibits that higher velocities and, consequently, higher shear rates are obtained by increasing ζ^*. The error incurred by using the simplified formulation drastically increases with increasing K. The reason is that at lower values of K the underestimation of the shear rate is accompanied by an underestimation of the mean velocity, leading to smaller errors in estimating the Poiseuille number. However, at higher values of K, the underestimation of the shear rate not only becomes more pronounced, but the mean velocity is also more precisely computed, resulting in more errors in evaluating the Poiseuille number. Figure 11b shows that, as expected, the simplified case supplies better estimations of the Nusselt number for higher K. The Nusselt number changes its sign from negative to positive as K increases from 1 to 10. This sign change is along with a singularity in the

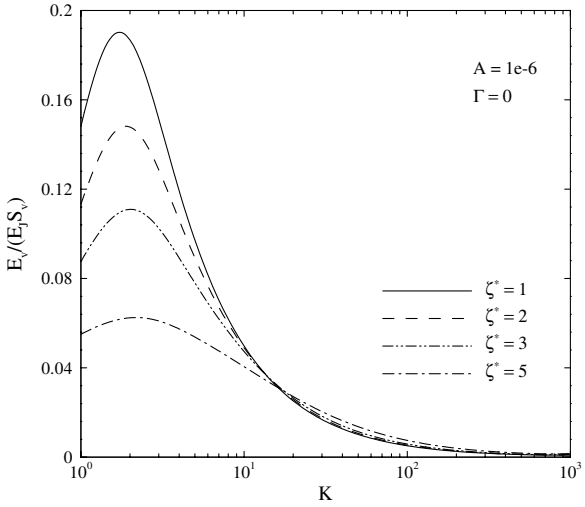

Fig. 10 $E_v/(E_J S_v)$ **as a function of** K **for purely electroosmotic flow.**

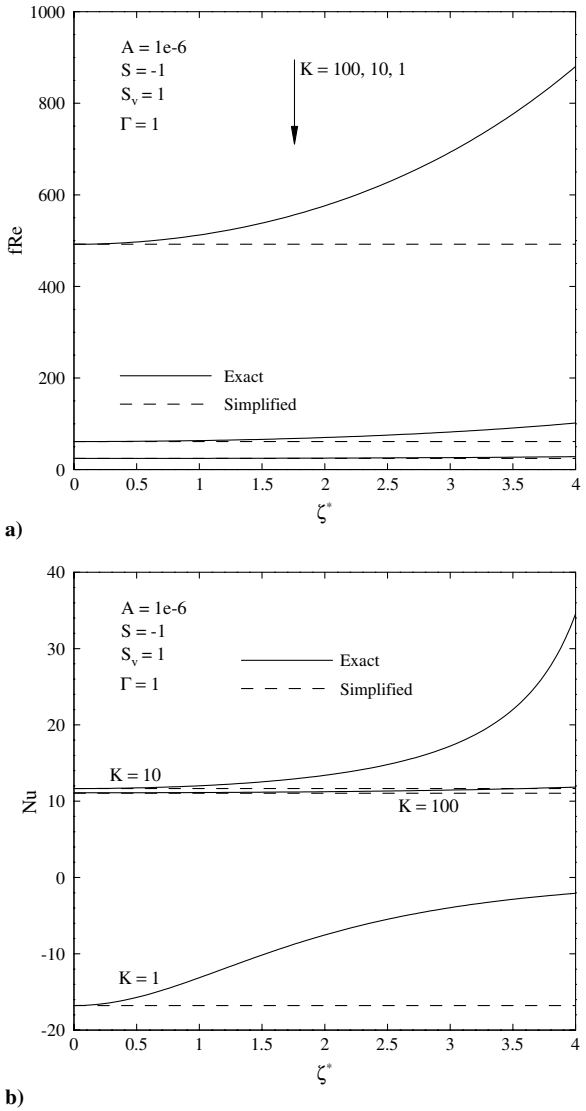

Fig. 11 Poiseuille number and Nusselt number versus dimensionless zeta potential at different values of K.

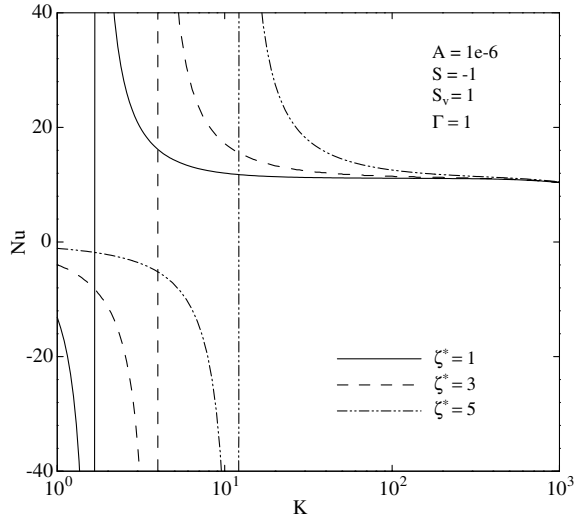

Fig. 12 Nusselt number as a function of K **at different dimensionless zeta potentials.**

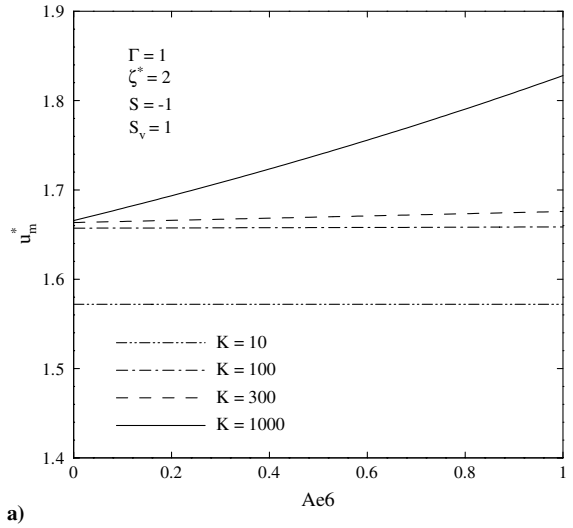

a)

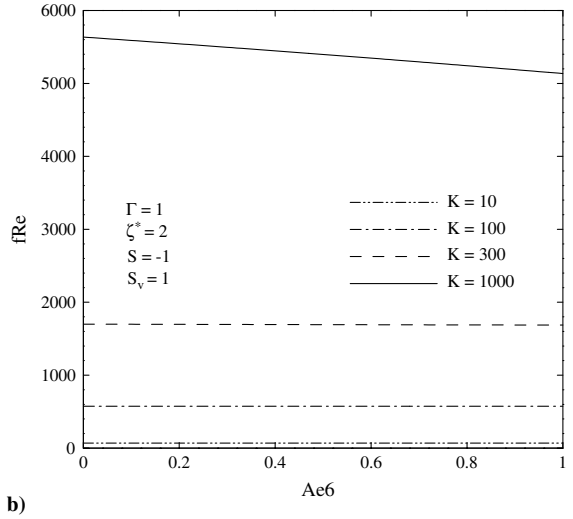

b)

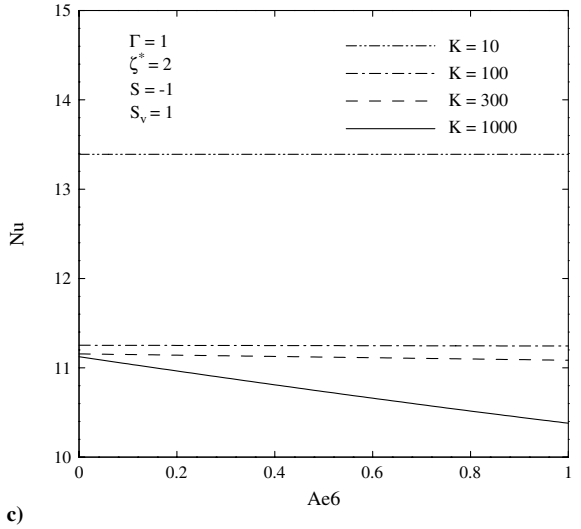

c)

Fig. 13 Dimensionless mean velocity, Poiseuille number, and Nusselt number versus the viscosity variation parameter.

Nusselt number values. Near the singularity point, the dimensionless bulk temperature attains low values, and even a small variation in the bulk temperature leads to considerable changes in the Nusselt number. Near the singularity points, the Debye–Huckel linearization may cease to be valid even for $\zeta^* < 1$, as it is for $K = 1$, which the error in evaluating the Nusselt number reaches about 18% at $\zeta^* = 0.8$. The error drastically increases by approaching the

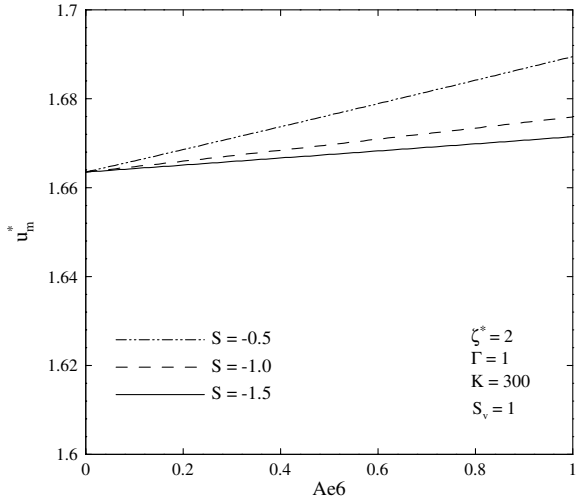

Fig. 14 Dimensionless mean velocity versus the viscosity variation parameter.

singularity point, which occurs at about $K = 1.6$ for this value of the dimensionless zeta potential and reaches approximately 103% at $K = 1.4$.

To make the source of this singularity clear, let us inspect Fig. 12, which depicts Nu versus K. At $K = 1$, the wall temperature is higher than the bulk temperature, resulting in a negative Nusselt number for a negative wall heat flux. The increase in K leads to increase in the velocity and, consequently, the energy transferred by the flow near the wall, resulting in a smaller temperature difference between the wall and the bulk flow. The final outcome is to increase the Nusselt number with negative sign. This trend lasts until the bulk and wall temperatures become the same. At this point, the heat transfer cannot be expressed in terms of the Nusselt number and a singularity occurs in the Nusselt number values. More increase in K makes the wall temperature fall a little below the bulk temperature, resulting in a great positive Nusselt number. By the above interpretation, it should now be obvious that the cause of the singularity point is grounded in the mathematical definition of the Nusselt number and not in the flow physics.

Figure 13 demonstrates the dimensionless mean velocity, Poiseuille number, and Nusselt number versus the viscosity variation parameter at different values of K. As observed, except for $K=$ 1000, the effects of the viscosity variation parameter on the flow parameters are negligible. For $K = 300$, the maximum error incurred by assuming constant fluid properties for u_m^*, fRe, and Nu are about 0.7, 0.7, and 0.6%, respectively. Although these values are drastically increased for $K = 1000$, however, as mentioned previously, this value of K is not encountered in the practical applications when the maximum allowable amount of A is present. Increasing the variations of the fluid properties with increasing K, while keeping the viscosity variation parameter constant, is not surprising. This condition implies that the channel height increases, and this leads to higher temperature differences and, consequently, higher property variations. The effect of the dimensionless Joule heating parameter on the changes of the dimensionless mean velocity due to the variations of the thermophysical properties is shown in Fig. 14. An increase in $|S|$ is accompanied by a decrease in temperature-dependent effects. This is due to the fact that a larger $|S|$ corresponds to a smaller wall heat flux and, consequently, smaller temperature differences throughout the channel cross section.

VI. Conclusions

A parametric study was carried out in this work to investigate combined effects of Joule heating, viscous dissipation, and variable thermophysical properties on mixed electroosmotically and pressure-driven flow in slit microchannels. The governing equations for fully developed conditions were made dimensionless and then solved by means of an implicit finite difference method. A discussion

based on the results obtained for practical applications was performed that gave the following conclusions:

1) To compute the velocity profile, the Debye–Huckel linearization may successfully be used up to $\zeta = 50$ mV. The accuracy of the results is higher for the pressure-assisted flow; however, special care should be taken when using this linearization for pressure-opposed flows with considerable amounts of the pressure gradient.

2) Even at moderate zeta potentials, the Poiseuille numbers obtained by means of the Debye–Huckel linearization may be quite different from the exact ones, especially at high values of K, which is the case for the majority of the practical applications.

3) Assuming a uniform distribution of the Joule heating leads to large errors in computing the thermal features for $\zeta^* > 1$, unless a sufficiently great value of the dimensionless Debye–Huckel parameter is considered.

4) Increasing the wall zeta potential decreases viscous heating effects at lower values of the dimensionless Debye–Huckel parameter, whereas the opposite is true for higher values of K.

5) For lower values of K, the effects of viscous heating for pressure-assisted flow is more pronounced than purely electro-osmotic flow and for the latter is also more pronounced than pressure-opposed flow.

6) The assumption of constant thermophysical properties can successfully be used for the majority of the practical applications. It was found that this assumption only fails at the extreme limits of the viscosity variation parameter and the dimensionless Debye–Huckel parameter, which are rarely encountered simultaneously in practice.

7) Increasing the dimensionless Joule heating parameter decreases the effects of variable thermophysical properties.

References

[1] Reuss, F. F., "Charge-Induced Flow," *Proceedings of the Imperial Society of Naturalists of Moscow*, Vol. 3, 1809, pp. 327–344.

[2] Burgreen, D., and Nakache, F. R., "Electrokinetic Flow in Ultrafine Capillary Slits," *Journal of Physical Chemistry*, Vol. 68, No. 5, 1964, pp. 1084–1091. doi:10.1021/j100787a019

[3] Rice, C. L., and Whitehead, R., "Electrokinetic Flow in a Narrow Cylindrical Capillary," *Journal of Physical Chemistry*, Vol. 69, No. 11, 1965, pp. 4017–4024. doi:10.1021/j100895a062

[4] Levine, S., Marriott, J. R., Neale, G., and Epstein, N., "Theory of Electrokinetic Flow in Fine Cylindrical Capillaries at High Zeta-Potentials," *Journal of Colloid and Interface Science*, Vol. 52, No. 1, 1975, pp. 136–149. doi:10.1016/0021-9797(75)90310-0

[5] Kang, Y., Yang, C., and Huang, X., "Dynamic Aspects of Electro-osmotic Flow in a Cylindrical Microcapillary," *International Journal of Engineering Science*, Vol. 40, No. 20, 2002, pp. 2203–2221. doi:10.1016/S0020-7225(02)00143-X

[6] Kang, Y., Yang, C., and Huang, X., "Electroosmotic Flow in a Capillary Annulus with High Zeta Potentials," *Journal of Colloid and Interface Science*, Vol. 253, No. 2, 2002, pp. 285–294. doi:10.1006/jcis.2002.8453

[7] Arulanandam, S., and Li, D., "Liquid Transport in Rectangular Microchannels by Electroosmotic Pumping," *Colloids and Surfaces, A: Physicochemical and Engineering Aspects*, Vol. 161, No. 1, 2000, pp. 89–102. doi:10.1016/S0927-7757(99)00328-3

[8] Xuan, X., and Li, D., "Electroosmotic Flow in Microchannels with Arbitrary Geometry and Arbitrary Distribution of Wall Charge," *Journal of Colloid and Interface Science*, Vol. 289, No. 1, 2005, pp. 291–303. doi:10.1016/j.jcis.2005.03.069

[9] Talapatra, S., and Chakraborty, S., "Double Layer Overlap in AC Electroosmosis," *European Journal of Mechanics, B/Fluids*, Vol. 27, No. 3, 2008, pp. 297–308. doi:10.1016/j.euromechflu.2007.06.005

[10] Talapatra, S., and Chakraborty, S., "Squeeze-Flow Electroosmotic Pumping Between Charged Parallel Plates," *International Journal of Fluid Mechanics Research*, Vol. 36, No. 5, 2009, pp. 460–472. doi:10.1615/InterJFluidMechRes.v36.i5.60

[11] Maynes, D., and Webb, B. W., "Fully Developed Electroosmotic Heat Transfer in Microchannels," *International Journal of Heat and Mass Transfer*, Vol. 46, No. 8, 2003, pp. 1359–1369. doi:10.1016/S0017-9310(02)00423-4

[12] Liechty, B. C., Webb, B. W., and Maynes, R. D., "Convective Heat Transfer Characteristics of Electro-Osmotically Generated Flow in Microtubes at High Wall Potential," *International Journal of Heat and Mass Transfer*, Vol. 48, No. 12, 2005, pp. 2360–2371. doi:10.1016/j.ijheatmasstransfer.2005.01.019

[13] Broderick, S. L., Webb, B. W., and Maynes, D., "Thermally Developing Electro-Osmotic Convection in Microchannels with Finite Debye–Layer Thickness," *Numerical Heat Transfer, Part A, Applications*, Vol. 48, No. 10, 2005, pp. 941–964. doi:10.1080/10407780500283309

[14] Iverson, B. D., Maynes, D., and Webb, B. W., "Thermally Developing Electroosmotic Convection in Rectangular Microchannels with Vanishing Debye–Layer Thickness," *Journal of Thermophysics and Heat Transfer*, Vol. 18, No. 4, 2004, pp. 486–493. doi:10.2514/1.3769

[15] Sharma, A., and Chakraborty, S., "Semi Analytical Solution of the Extended Graetz Problem for Combined Electroosmotically and Pressure Driven Microchannel Flows with Step Change in Wall Temperature," *International Journal of Heat and Mass Transfer*, Vol. 51, Nos. 19–20, 2008, pp. 4875–4885. doi:10.1016/j.ijheatmasstransfer.2008.02.041

[16] Mala, Gh. M., Li, D., Werner, C., Jacobasch, H. J., and Ning, Y. B., "Flow Characteristics of Water Through a Microchannel between two Parallel Plates with Electrokinetic Effects," *International Journal of Heat and Fluid Flow*, Vol. 18, No. 5, 1997, pp. 489–496. doi:10.1016/S0142-727X(97)80007-0

[17] Yang, C., and Li, D., "Analysis of Electrokinetic Effects on the Liquid Flow in Rectangular Microchannels," *Colloids and Surfaces, A: Physicochemical and Engineering Aspects*, Vol. 143, Nos. 2–3, 1998, pp. 339–353. doi:10.1016/S0927-7757(98)00259-3

[18] Yang, C., Li, D., and Masliyah, J. H., "Modeling Forced Liquid Convection in Rectangular Microchannels with Electrokinetic Effects," *International Journal of Heat and Mass Transfer*, Vol. 41, No. 24, 1998, pp. 4229–4249. doi:10.1016/S0017-9310(98)00125-2

[19] Chakraborty, S., "Analytical Solutions of Nusselt Number for Thermally Fully Developed Flow in Microtubes Under a Combined Action of Electroosmotic Forces and Imposed Pressure Gradients," *International Journal of Heat and Mass Transfer*, Vol. 49, Nos. 3–4, 2006, pp. 810–813. doi:10.1016/j.ijheatmasstransfer.2005.07.048

[20] Das, S., and Chakraborty, S., "Effect of Conductivity Variations Within the Electric Double Layer on the Streaming Potential Estimation in Narrow Fluidic Confinements," *Langmuir*, Vol. 26, No. 13, 2010, pp. 11589–11596. doi:10.1021/la1009237

[21] Maynes, D., and Webb, B. W., "The Effect of Viscous Dissipation in Thermally Fully Developed Electroosmotic Heat Transfer in Microchannels," *International Journal of Heat and Mass Transfer*, Vol. 47, No. 5, 2004, pp. 987–999. doi:10.1016/j.ijheatmasstransfer.2003.08.016

[22] Sadeghi, A., and Saidi, M. H., "Viscous Dissipation Effects on Thermal Transport Characteristics of Combined Pressure and Electroosmotically Driven Flow in Microchannels," *International Journal of Heat and Mass Transfer*, Vol. 53, Nos. 19–20, 2010, pp. 3782–3791. doi:10.1016/j.ijheatmasstransfer.2010.04.028

[23] Tang, G. Y., Yang, C., Chai, C. K., and Gong, H. Q., "Numerical Analysis of the Thermal Effect on Electroosmotic Flow and Electrokinetic Mass Transport in Microchannels," *Analytica Chimica Acta*, Vol. 507, No. 1, 2004, pp. 27–37. doi:10.1016/j.aca.2003.09.066

[24] Holman, J. P., *Heat Transfer*, 9th ed., McGraw–Hill, New York, 2002.

[25] Probstein, R. F., *Physicochemical Hydrodynamics*, 2nd ed., Wiley, New York, 1994.

[26] Dandapat, B. S., Santra, B., and Vajravelu, K., "The Effects of Variable Fluid Properties and Thermocapillarity on the Flow of a Thin Film on an Unsteady Stretching Sheet," *International Journal of Heat and Mass Transfer*, Vol. 50, Nos. 5–6, 2007, pp. 991–996. doi:10.1016/j.ijheatmasstransfer.2006.08.007

[27] Lide, D. R., *CRC Handbook of Chemistry and Physics*, 88th ed., CRC Press, Boca Raton, FL, 2008.

[28] Karniadakis, G., Beskok, A., and Aluru, N., *Microflows and Nanoflows, Fundamentals and Simulation*, Springer, New York, 2005.